Characterization of X-ray Damage to Perfluorosulfonic Acid Using Correlative Microscopy

Isaac Martens,[†,∥] Lis G. A. Melo,[§,∥,⊥] David P. Wilkinson,[‡] Dan Bizzotto,[†] and Adam P. Hitchcock*,[§]

†Department of Chemistry and ‡Department of Chemical Engineering, University of British Columbia, Vancouver V6T 1Z1, BC, Canada

§Department of Chemistry & Chemical Biology, McMaster University, Hamilton L8S 4M1, ON, Canada

Ⓢ Supporting Information

ABSTRACT: Polymer electrolytes such as perfluorosulfonic acid (PFSA) are key to a variety of electrochemical and clean energy applications. Many analytical techniques for characterizing nanostructured devices containing polymer electrolytes use high-energy electrons or X-rays, which can severely damage soft matter. To better analyze these materials, it is important to understand the chemical, physical, and spectroscopic changes that occur due to radiation damage. Soft X-ray damage to PFSA was characterized using a combination of X-ray microscopy, X-ray absorption spectroscopy, infrared spectroscopy, fluorescence imaging, and atomic force microscopy. X-ray exposure induces substantial and selective loss of fluorine, preferential cleavage of the side chains, and physical ablation of the polymer. The combination of multiple imaging and spectroscopy modalities provides detailed insight into radiation damage mechanisms.
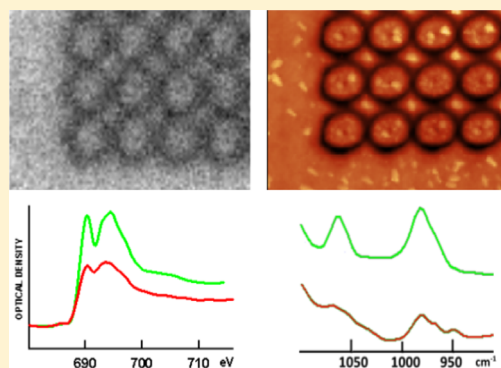
1. INTRODUCTION

Polymer electrolytes are widely used in electrochemical devices, although their precise morphology and distribution remains poorly understood.[1,2] Proton-conducting perfluorosulfonic acid (PFSA) ionomers (e.g., Nafion) are critical for the operation of proton exchange membrane (PEM) hydrogen fuel cells in particular. The precise hydrated structure of PFSA inside fuel cell catalyst layers has attracted much attention over several decades.[1,3−5] Recently, synchrotron X-ray[6−8] and electron microscopy[9,10] techniques have been used to probe the morphology of PFSA dispersed as proton-conducting ionomer and binder inside Pt/C nanoparticle catalyst films. Scanning transmission X-ray microscopy (STXM) is especially useful for analysis of composite materials with one or more polymer components.[11,12] It provides a good spatial resolution (ca. 25−30 nm) and quantitative elemental/chemical speciation capabilities,[13,14] combined with a damage rate relative to analytical outcome that is several orders of magnitude lower than analytical electron microscopy.[8,15,16]

The push to characterize the nanoscale morphology of ionomer with increased detail and in three dimensions intrinsically exposes samples to higher doses of ionizing radiation. Although PFSA is chemically quite inert, it is extremely sensitive to X-ray and electron beam damage.[8−10,17−20] More than 70% of the ionomer volume in a sample can be lost during high-resolution, multielement, tomographic soft X-ray imaging,[21] and an even larger fraction can be lost with analytical electron microscopy.[8] The use of cryo-microscopy conditions somewhat reduces, but does not

prevent, radiation damage to PFSA.[10,19] Mitigating the effects of beam damage, while achieving useful analytical results, is one of the key objectives in the ongoing development of reliable, quantitative methods for mapping PFSA in PEM fuel cell samples.[21−23]

Improving the durability of PEM fuel cells remains a major technical challenge. A large fraction of fuel cell research is therefore devoted to understanding the electrochemical degradation phenomena of the different components and the long-term stability of devices.[24,25] Optimization of the spatial distribution and stability of the PFSA ionomer in the cathode is of great interest but is impeded by radiation damage. Electron and X-ray microscopies have been used to elucidate the structural evolution of the Pt,[26] carbon support,[27] and PFSA[28] components associated with fuel cell performance degradation. It is critical that any damage induced by the probe beam is minimized when analyzing partially degraded or end-of-life fuel cell samples, and that radiation damage effects can be distinguished from electrochemical corrosion, aging, and other degradation phenomena such as carbon corrosion.[27] Some aspects of the radiation damage processes may also shed light on the radical-induced degradation mechanisms of PFSA during electrochemical testing.

A more systematic understanding of beam-induced chemistry and the dose−damage relationship is necessary to

optimize data collection strategies and quantitative interpretation of analytical microscopy data. The mechanisms of radiation damage of PFSA are poorly understood. The chemistry and morphology of PFSA are modified by ionizing radiation, and there is significant fluorine loss.[8−10,18,20,21,29] Vibrational spectroscopy has been used to show that X-rays cause formation of unsaturated C and O species and scission of C−O and C−S bonds.[18] X-ray photoelectron spectroscopy (XPS) has been interpreted to indicate that X-ray-induced decomposition of side chains is favored over changes to the poly(tetrafluoroethylene) (PTFE) backbone.[17] Reduced proton conductivity of X-ray-damaged PFSA is consistent with cleavage of the sulfonic acid or ether moieties.[30] STXM studies of damage by 320 eV X-rays to PFSA showed that the dominant outcomes are significant modification of the $-(CF_2-CF_2)-$ geometry and electronic structure, accompanied by fluorine mass loss.[20,29] However, STXM measurements could not determine if X-ray damage to the side chain occurred faster or slower than damage to the backbone.[29] While these studies have identified radiation damage effects qualitatively,[17,18,30] the quantitative dose dependence of these processes has only recently been addressed.[8,19−21,29,31]

This study has characterized the chemical and morphological changes in PFSA induced by soft X-rays by combining near-edge X-ray absorption fine structure spectroscopy (NEXAFS) with nondestructive microanalysis by Fourier transform infrared (FTIR) spectromicroscopy and atomic force microscopy (AFM). First, a scanning transmission X-ray microscope (STXM) was used to expose PFSA films with controlled radiation doses at precise locations. Then, NEXAFS images were collected at these locations without removing the sample from the STXM microscope. This in situ approach has been used extensively to study the spectral and thus chemical changes, and to quantify dose−damage relationships, for a variety of polymeric materials.[32−37] After dosing and in situ NEXAFS characterization, the sample with the dosed regions was removed, transported to a distant laboratory, and then examined ex situ with FTIR and AFM techniques to investigate the chemical and structural evolution of irradiated PFSA.

2. MATERIALS AND METHODS

2.1. Sample Preparation. PFSA films of uniform thickness were prepared by spin coating. A 5 wt % Dupont D521 ionomer solution (EW 1100, protonated form, Ion Power Inc.) was diluted with isopropanol (99.5%, Caledon Laboratory Chemicals) to 2 wt %. Approximately 100 μL of this solution was deposited dropwise on to a ~1 cm² cleaved mica substrate until it was covered. The solution-coated mica was then spun using a 6708D spin coater (Specialty Coating Systems), operated at 4500 rpm for 30 s under ambient temperature and pressure. After spin coating, the polymer on the mica was scored into small ~1 mm² squares using a clean scalpel blade. The PFSA film was then floated from the mica onto the surface of distilled water, previously cleaned by passing lens paper over the surface. Floating pieces of film were transferred onto a 75 nm thick silicon nitride (SiN$_x$) window (Norcada Inc).

2.2. X-ray Exposure. STXM irradiation and analytical measurements were carried out using either the polymer STXM[38] at beamline 5.3.2.2[39] at the Advanced Light Source (ALS) in Berkeley, California, or the ambient STXM at beamline 10ID1[40] at the Canadian Light Source (CLS) in Saskatoon, Canada. The SiNx wafer sample was taped to a standard Al trapezoidal holder. The STXM chamber was evacuated to approximately 100 mbar and then backfilled with He to 1/3 atm at ALS 5.3.2.2 and 1/6 atm at CLS 10ID1. The X-ray dose was controlled by modifying the incident X-ray flux, the size of the beam, the pixel spacing, and the exposure time on the sample. The damage energy was 320 eV, chosen to be far from any spectroscopic features and at an energy where all carbon atoms in the sample absorb.

Large areas of PFSA samples (between 250 and 900 μm²) were damaged with X-rays using multipoint irradiation with the STXM scanner operated in point-by-point mode. The pixel step size and beam spot diameter were both 500 nm. The zone plate position (controlled by adjusting A_0, which is the separation of the order sorting aperture (OSA) and the sample) was adjusted to ensure precise defocusing.[29] Supporting Figure S-1 illustrates that for a 500 nm spot size, the inner ~200 nm of the spot is not illuminated by X-rays in the case of a perfect zone plate and perfect lens−OSA alignment. The annular shape of each spot reflects the projected intensity profile of a defocused Fresnel zone plate (see Supporting Information Section SI.1). The absorbed dose was calculated using a simplified version of a previously described method[31] considering that the spot is an annulus as shown in Figure S-1 (see Supporting Information (SI) Section SI.1 for details). The detector efficiency was determined using the lithographic transition in PMMA.[34] Three regions were damaged with X-rays, one with a high nominal dose (47 MGy; region C) and two at lower nominal doses (5 and 6 MGy; regions A and B, respectively). A fourth region, visible in some images, received a nominal dose 12 MGy (region D).

2.3. STXM and NEXAFS. In STXM imaging, a thin specimen is raster-scanned in the X direction and step-scanned in the y-direction,[38] while the sample is positioned in the Z-direction at the focus (or a controlled displacement from focus) of a monochromated X-ray beam. Images are recorded pixel by pixel by detecting the transmitted X-rays using a phosphor to downconvert X-rays to visible photons, which are detected in single-event counting mode using a photomultiplier detector. Details regarding instrumentation,[38] data acquisition, and analysis[13] can be found elsewhere. The measured transmission images are converted to optical density images using the Beer−Lambert law, $OD = -\ln(I/I_o)$, where I_o is the X-ray intensity measured through the supporting SiN$_x$, but without the sample, and I is the X-ray intensity transmitted through the sample and SiN$_x$ support. The OD spectrum is related to the sample properties: $OD(x, y, E) = \mu(E) \rho t(x, y)$, where $\mu(E)$ is the mass absorption coefficient at energy E, ρ is the density, and $t(x, y)$ is the thickness of the sample at the (x, y) pixel. The spin-coated PFSA film was 50(5) nm thick, as measured by X-ray absorption.[13,41] It was uniformly thick to <10 nm over a macroscopically large area (>0.1 × 0.1 mm).

After the X-ray exposure, C 1s, O 1s, and F 1s NEXAFS spectra of the three damaged areas as well as the undamaged film were collected using image sequences (also called stacks[42]) measured under low-damage conditions. The NEXAFS stacks imparted an additional 3 MGy. A check for radiation damage was done after each stack by collecting a lower-magnification, high-contrast image at 292.4 eV (the C 1s photon energy where PFSA is most sensitive to radiation damage) over the stack area and some of the surrounding, nonirradiated area. Changes in absorbance of less than 5% were considered to be negligible damage.

Table 1. Quantitative Changes in C, O, and F Elemental Amounts due to Soft X-ray Damage Evaluated by NEXAFS Spectral Changes

area[a]	I_o	time	dose (MGy)[b]		% difference to undamaged area		
	MHz	ms	nominal	imparted	C 1s	O 1s	F 1s
A (4)	7.2	300	5	7	5 (1)	4 (1)	7 (1)
B (1)	7.2	700	6	9	−3 (1)	10 (1)	13 (1)
C (2)	7.2	7000	47	70	3 (1)	11 (1)	38 (4)
D (3)	15.7	300	12	16			

[a]Area A was irradiated at CLS ambient STXM on beamline 10ID1 using a measured flux of 7.2 MHz at 320 eV, or 22 MHz, taking into account the 32% detector efficiency. Areas B, C, and D were irradiated at the ALS polymer STXM on beamline 5.3.2.2 using a measured incident flux of 7.2 MHz at 320 eV, or 22 MHz, taking into account the detector efficiency. In each case, the step size was 500 nm, and the beam was defocused to 500 nm. See Supporting Section S-1 for a discussion of beam size and how the dose was evaluated. For A, B, and C, the dose was varied by changing the dwell time that the defocused beam was stationary at each pixel. For D, the incident flux was increased. [b]Nominal dose corresponds to that assuming the irradiation was uniform over the full area, while imparted dose is the dose to the annulus actually irradiated by the defocused beam (see Supporting Section S-1). The nominal dose is the relevant quantity for the quantitative evaluation of the X-ray damage since those results are based on analysis of spectra averaged over the whole damaged area, not just the high-dose annulus.

X-ray damage in terms of both elemental and chemical changes was quantified by comparison of the spectrum of the damaged areas to that of the undamaged PFSA. Elemental changes were evaluated as follows. First, the spectrum of the damaged area was converted to wavelength. A linear background extrapolated from the pre-edge signal was then subtracted to remove the contribution of other elements that absorb X-rays but do not contribute to the edge signal. After converting back to energy scale, the background-subtracted spectra were integrated from 280 to 340 eV for C 1s, 520 to 560 eV for O 1s, and 680 to 730 eV for F 1s. Table 1 quantifies the elemental changes to the PFSA caused by soft X-ray irradiation. Changes to the intensity of specific transitions were evaluated by taking the OD at the peak energy for each edge and subtracting the OD from a pre-edge energy (i.e., for C 1s, $(OD_{292.4} - OD_{280})$, for O 1s $(OD_{540} - OD_{525})$, and for F 1s $(OD_{690} - OD_{684})$. The percent differences between the peak OD of regions A, B, and C and that of undamaged PFSA are listed in Table 2. All data analyses were performed using aXis2000 software.[43]

Table 2. Quantitative X-ray Damage-Induced Changes of the Intensities of Specific NEXAFS Transitions

area	% OD difference[a] relative to undamaged area		
	292.4 eV (C-F)	540 eV (C-O)	690 eV (F-C)
A	3 (1)	11 (1)	8 (1)
B	10 (1)	12 (1)	11 (1)
C	32 (2)	17 (2)	40 (4)

[a]The pre-edge signal at 280 eV (C 1s), 526 eV (O 1s), and 684 eV (F 1s) was subtracted from OD_E.

One complication of the use of defocused spots from a zone plate lens is that, after about 200 nm defocus, the photon distribution becomes an annulus, and more of the dose is delivered in that annulus compared to the dose inside the annulus, which is the shadow of the central stop of the zone plate. Supporting Figure S-2 shows this phenomena for region C, which received a nominal dose of 47 MGy delivered at 320 eV, which is deposited mostly in the annulus. Although the central part should not have received any dose, Figure S-2 shows that it received a dose of about 50% of that delivered to the annulus. This is because there is a significant component of the X-ray intensity outside the direct geometric projection of the zones due to the Airy function of the diffractive focus. The

signal outside of the central part of the Airy distribution is roughly 50%, in agreement with the extent of damage (Figure S-2c). Note that STXM allows for a postdamage analysis of both the annulus and the surrounding regions, while the FTIR signal is averaged over the entire damaged region.

2.4. FTIR Spectromicroscopy. Transmission mode spectra were measured using an Equinox 55 spectrometer and a Hyperion microscope (Bruker). The microscope was equipped with an MCT detector and 36× objective lens (Coherent Inc., NA 0.5). All spectra were acquired at 8 cm⁻¹ resolution. To improve signal-to-noise ratio while minimizing drift, background and sample point spectra were measured in an interleaved fashion. A total of 512 scans were collected at each position immediately one after another. Absorbance spectra from each sequential pair of background and sample measurements were normalized at the baseline to correct offsets, then averaged with 6−10 replicates. Error bars on integration plots represent the standard deviation between integrals of replicates for each peak. Details on the peak integration and background scattering correction can be found in the Supporting Information Section SI.3. Alignment between the optical and IR light paths was checked using an electron microscopy grid. The scanner velocity was 20 kHz, with double-sided acquisition and a 16 kHz low-pass filter. The samples were mounted and left to equilibrate in a dry air stream inside the microscope for several days before measurements. The absorbance of each region was normalized to the local thickness of the film determined from STXM.

2.5. Atomic Force Microscopy (AFM). Tapping mode images were collected on an Agilent 5500 atomic force microscope equipped with a 90 × 90 μm scanner. Silicon nitride tips were used as received (170 kHz AAC, Agilent). The images were collected at a maximum of 2 μm/s, at the highest possible gain without inducing ringing artifacts. To check for tip-sample damage, 19 sequential 1 × 1 μm frames were recorded. No visible differences between the images were detected (Figure S-3). Experiments were performed under ambient humidity (~24% RH). All images were processed using Gwyddion software[44] and Fiji from Image J.[45] A three-point level was applied before extracting linescans. Further details are given in Supporting Information Section SI.4.
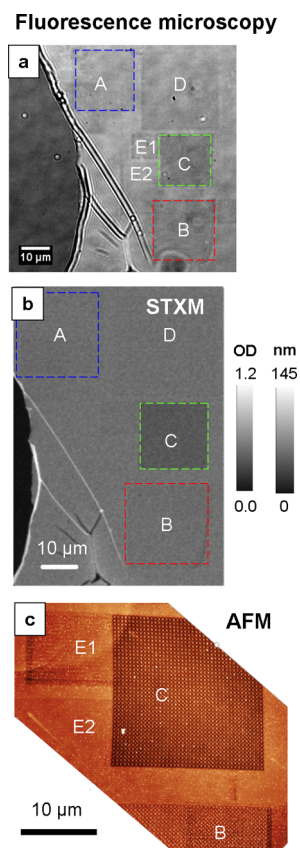
2.6. Fluorescence Microscopy. Fluorescence images were collected using an Olympus IX70 microscope in transmission mode equipped with an EM-CCD Evolve digital camera. LED

excitation at 375 nm was combined with a 515−550 nm emission filter.

3. RESULTS

3.1. Physical Morphology of X-ray-Damaged PFSA.
Figure 1 shows images of the three X-ray dosed regions using

Figure 1. Images of a perfluorosulfonic acid (PFSA) spin-coated film damaged by 320 eV soft X-rays imaged by (a) UV-excited fluorescence microscopy, (b) optical density (OD) scanning transmission X-ray microscopy (STXM) at 292.4 eV (the C 1s → σ^*_{C-F} transition at which the spectrum is particularly damage-sensitive), and (c) atomic force microscopy (AFM) topography. Areas A, B, and C received 5, 6, and 47 MGy nominal dose, respectively. Area D (to the right of A) received 15 MGy, while areas E1 and E2, to the left of C, received <3 and <2 MGy (areas E1 and E2 were used to take multiple images of area C using large defocus).

fluorescence microscopy (Figure 1a), STXM (OD at 292.4 eV; Figure 1b), and AFM (topography mode; Figure 1c). While the spatial resolution, probe−sample interactions, and operating principles of the three techniques are very different, the three damaged regions that received nominal doses of 5, 6, and 47 MGy (areas A, B, and C, respectively) are clearly visible in all three types of images.

Acid-form PFSA samples exposed to laboratory environments spontaneously accumulate volatile organic contaminants.[46] Membranes stored in open air eventually turn dark brown from acid-catalyzed polymerization[47] and become weakly fluorescent. X-ray exposure bleaches this fluorescence. Fluorescence microscopy with near-ultraviolet excitation images this trace contamination on ionomer samples after X-ray exposure (Figure 1a). Regions exposed to low X-ray doses (<4 MGy, i.e., areas E1 and E2) are dark, indicating

photobleaching. The fluorescence signal did not recover even after storage in air for 1 year after X-ray dosing.

The thicknesses of several areas of the undamaged PFSA film were determined by AFM topography measurements over the edge of the film. The AFM thickness results (55 ± 5 nm) agreed with those determined by STXM (50 ± 5 nm). The slightly larger thickness determined by AFM could be due to adsorption of ambient moisture since AFM was performed on samples that had been equilibrated with humid air in Vancouver for many days, while the STXM data were acquired under dry He at reduced pressure. Thicknesses measured by AFM over the edge of the film also assumes the sample lies perfectly flat against the substrate.

Figure 2 presents higher-resolution STXM images (Figure 2a,b) and AFM topographic (Figure 2c,d) and phase (Figure
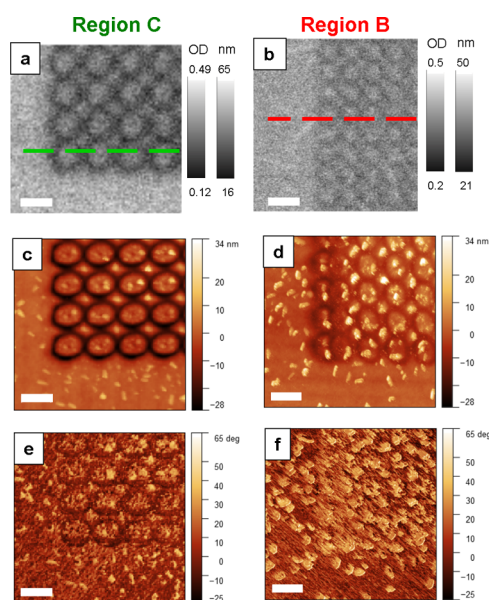
Figure 2. High-resolution STXM and AFM images of the PFSA-damaged areas C (left column) and B (right column). (a, b) STXM OD images at 292.4 eV of regions C and B. (c, d) AFM topography images. (e, f) AFM phase contrast images. All scale bars are 500 nm.

2e,f) images of regions B and C. Instead of uniformly exposed circular areas with 500 nm diameter, spaced 500 nm apart, distorted annular areas are clearly visible in both damaged areas with both techniques. The distortion from the ideal circular shape reflects the spatial distribution of the defocused X-ray spot used to damage these areas (see Supporting Section SI.1). Linescans quantifying the radiation-induced changes in thickness using both techniques are shown in Figure 3. The STXM images show that region C, which received a nominal dose of 47 MGy (Figure 2a), produced depressions of approximately 15 nm depth in the central part of each spot and ~18 nm in the most heavily damaged annulus, decreasing the film thickness by 30−40% (Figure 3a). Region B (Figure 2b), which received a nominal dose of 6 MGy, shows shallower, ~5 nm depressions (~10% of thickness lost), with less edge definition (Figure 3b).

AFM shows that soft X-ray damage causes substantial changes to the surface morphology of the PFSA film. Figure 2c,d displays the topography of regions C and B, respectively. Figure 2c shows that each STXM pixel (step size) of region C leaves an annulus with sunken edges (Figure 2c). Similar
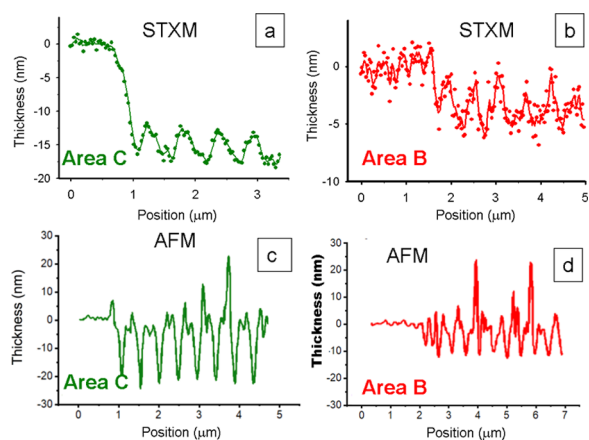
Figure 3. Line profiles from the STXM and AFM images (lines indicated in Figure 2a,b). Line profile of STXM OD image at 292.4 eV shown in (a) Figure 2a of damaged region C and (b) Figure 2b of damaged region B. Line profile of AFM topography image as shown in (c) Figure 2c of damaged region C and (d) Figure 2d of damaged region B.

shaped, but shallower annular features are seen in region B (Figure 2d). Higher doses ablate deeper holes into PFSA, as seen in Figure 3c. In this extracted linescan, the roughness was smoothed over the width of one STXM pixel of damage (500 nm) to highlight the average ablation. Damage was also detected in regions over which the postexposure NEXAFS images were acquired, visible as rectangles shown as regions E1 and E2 (Figure 1c). The depth of polymer ablation (∼3 nm) in these analysis stack areas is consistent with the estimated dose (∼3 MGy), which was less than in the areas given nominal doses of 5, 6, and 47 MGy (∼5, 5, and 13 nm, respectively). Ablation depth was measured halfway between peak and trough. The average ablation observed by AFM is in agreement with that measured by STXM NEXAFS (Figure 3), but shows better sensitivity and spatial resolution.

The shape of each annulus reflects the projected intensity profile of a defocused Fresnel zone plate (see Section SI.1). The dose in the heavily damaged annulus areas, called the imparted dose, is higher than the nominal dose, which assumes the illumination is uniform over a 500 nm diameter spot. Using the dose formula presented in Supporting Section S.1, the imparted doses of regions A, B, and C were 7, 9, and 70 MGy, respectively. These values are significantly larger than the nominal dose values. Despite nonuniform illumination with defocused beams larger than 200 nm, as long as the step (pixel) size is as large or larger than the defocused spot size, high-quality, multielement NEXAFS images can be collected with negligible beam damage.

A large number of particles are seen in the AFM topography (Figure 2c,d) and especially the AFM phase images (Figure 2e,f). The high contrast of the particles in the AFM phase images (Figure 2e,f) indicates that the particles have a very different viscoelastic response compared to undamaged PFSA. Raised bubble-like features are visible, similar to internal voids generated in electron-beam-damaged specimens.[9] Since relatively few particles are observed 10's of microns away from the X-ray-damaged areas, it is natural to interpret these particles as "ejecta"—ablated material redeposited onto nearby areas. Radiation-induced mass loss of small-intact fragments from PTFE has been demonstrated by mass spectrometry.[48] In addition to particles on the areas A, B, and C damaged using a

defocused beam, a region of the PFSA film was damaged using a fully focused X-ray beam (nominal 30 nm beam spot size) with 500 nm pixel step size. AFM of this area (Figure S-4) showed that the fully focused beam created much deeper ablation artifacts, similar to those seen in region C.

Particulate material in the areas of regions A, B, and C was visible in STXM images recorded at 292.4 and 320 eV, a year after the AFM images were measured (see Figure S-5). The needlelike particles in the STXM images in Figure S-5 are typically ca. 1−2 μm long, ∼100 nm wide, and 30 nm tall. The particles observed by STXM are much larger than the particles observed by AFM, and the morphology is quite different. This suggests that some or perhaps most of these particles might have been deposited on the damaged areas, due to electrostatic charge caused by the damage and fluorine loss. The AFM images were only measured weeks after the STXM irradiation and after the sample had been subjected to drying for several days in a flow of lab air in the FTIR microscope.

A follow-up experiment was carried out to determine if these particles are indeed "ejecta" associated with the X-ray damage. Since particles were observed by STXM in regions B and C, we would expect to see similar size and distribution of particles if an area subjected to similar irradiation conditions was measured using fully focused high-resolution STXM imaging immediately after irradiation and without removing the sample from the STXM. A previously unexposed area of the same PFSA sample was exposed using exactly the same dosing conditions as used for area C (see Figure 1) (for details, see caption to Figure S-6). This freshly damaged area was then examined by STXM using fully focused beam and 5 ms dwell time to improve statistics, while the sample was still in the STXM microscope chamber. STXM OD images at 292.4 eV (showing the array of damage spots caused by the 500 nm defocused beam) and at 320 eV (sensitive to total thickness) are presented in Figure S-6. No particles were observed. After this follow-up STXM experiment, the sample was transported by air to UBC where it was immediately examined using the same AFM used previously. An AFM topography image is shown in Figure S-6c, along with the 292.4 eV STXM image cropped to approximately the same area (Figure S-6d). While particles were observed by the much higher spatial resolution AFM (Figure S-6e), they were very much smaller (10−15 nm; see Figure S-6f) and less numerous than the particles observed in area C of the original study. At present, we cannot prove unambiguously that "ejecta" particles are generated by X-ray damage to the PFSA sample. Nor can we rule out the possibility that postirradiation particle contamination occurs in X-ray-irradiated regions, perhaps due to electrostatic charging. Clearly, the possibility of such particle ejection could significantly affect quantitative dose−damage studies. The occurrence of "ejecta" phenomena should be monitored using sufficiently high-resolution and sensitive imaging such as AFM, further validating the correlative microscopy approach used in the present study. It is noteworthy that the dosing conditions used in this damage study are very different from those used in regular STXM operation, where typically 1−3 ms dwell time/pixel are used.

3.2. Inner Shell Spectroscopy of PFSA and Radiation-Damaged PFSA. The following is a brief summary of the main features of the spectra of undamaged PFSA[49] and more detailed discussion of the NEXAFS images of X-ray-damaged PFSA.[20,29] The C 1s, O 1s, and F 1s NEXAFS images of undamaged PFSA and the damaged areas A, B, and C are

shown in Figure 4. Low nominal doses of 5 or 6 MGy (regions A and B) cause barely detectable changes to the C 1s
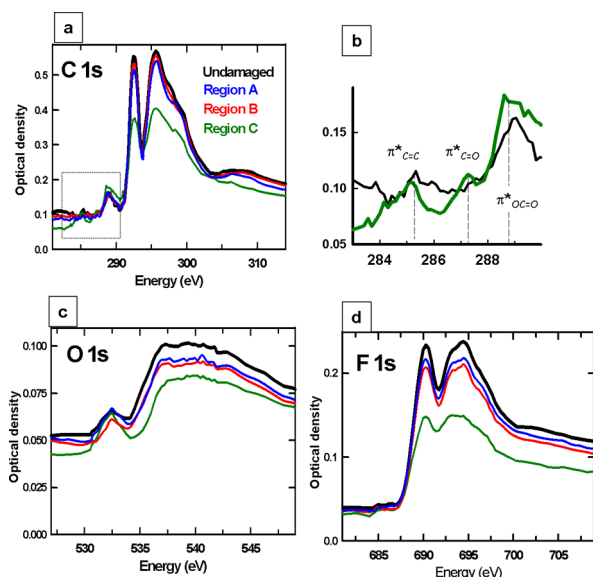

Figure 4. NEXAFS images of undamaged and X-ray-damaged PFSA. (a) C 1s spectra and (b) expanded region from 283 to 290 eV of the C 1s spectra. (c) O 1s spectra and (d) F 1s spectra for the undamaged and X-ray-damaged areas A, B, and C.

spectrum, while notable differences are seen in the F 1s spectra. The spectra of region C (47 MGy) shows substantial changes in the NEXAFS images at all three edges. There is a strong decline in the C 1s peaks at 292.6 and 296 eV (Figure 4a) and in the F 1s peaks at 689 and 694 eV (Figure 4d). These features are excitations to (1s, $\sigma^*_{C-F}(\perp)$) and (1s, $\sigma^*_{C-F}(//)$) states associated with $-(CF_2-CF_2)-$ regions in the backbone and side chains of PFSA.[49] There is also a decay of the broad C 1s $\rightarrow \sigma^*_{C-C}$ feature at 307 eV.[49] New peaks appear in the C 1s edge at 285.3 and 287 eV (Figure 4b). These peaks are most likely C 1s(C=C) $\rightarrow \pi^*_{C=C}$ and C 1s(C=O) $\rightarrow \pi^*_{C=O}$ transitions[50] consistent with the formation of C=C and C=O bonds. Changes to the F 1s spectrum are the most prominent and are consistent with two phenomena:[29] (i) fluorine loss, which decreases the intensity of the fluorine 1s excitations at 690 and 694 eV as well as the C 1s pre-edge signal and the F 1s continuum; and (ii) amorphization of the $-(CF_2-CF_2)-$ structure such that the 690 and 694 eV (1s^{-1}, $\sigma^*_{C-F}(\perp)$) and (1s^{-1}, $\sigma^*_{C-F}(//)$) peaks are significantly decreased. At even higher doses, these two peaks disappear and are replaced by a single, broad peak at 692 eV.[20] The fluorine loss results in reduction of the fluorine valence ionization continuum, which underlies both the C 1s and O 1s spectra. At the O 1s edge (Figure 4c), the broad peak between 535 and 545 eV is attributed to the overlap of the O 1s(C−O) $\rightarrow \sigma^*_{C-O}$ transition at the ether bond and O 1s(S−O) $\rightarrow \sigma^*_{S-O}$ transitions.[49] Even with low doses (regions A and B), the intensities of these peaks are visibly reduced. Note that in more detailed studies of X-ray-damaged PFSA,[20,29] there was clear evidence for highly volatile oxygen impurities (possibly entrapped solvent from the spin coating) so that the changes to the O 1s spectra in the lightly damaged areas A and B could be related to changes in the oxygen-containing impurities, rather than to PFSA itself.

3.3. FTIR Spectroscopy of PFSA and Radiation-Damaged PFSA. Figure 5 presents FTIR spectra of the
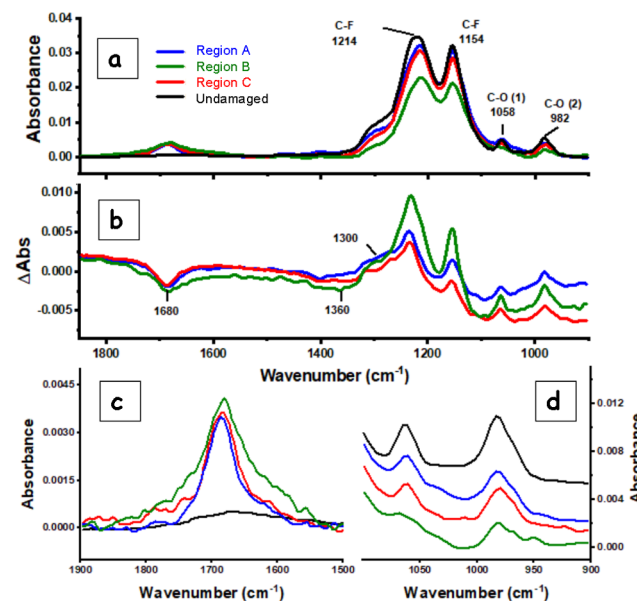
Figure 5. (a) FTIR absorbance spectra of reference (undamaged) and X-ray-exposed PFSA. (b) Differential absorbance FTIR spectra of damaged versus undamaged PFSA. (c) Magnification of the FTIR differential absorbance in C−O region. The signal is inverted. (d) Magnification of the FTIR differential absorbance in C=O region.

undamaged and X-ray-damaged PFSA areas, A, B, and C, compared to that of undamaged PFSA. Supporting Figure S-7 presents the FTIR spectrum of the SiN$_x$ window showing that it presents negligible interference. Supporting Figure S-8 presents the full range (3000−800 cm^{-1}) of the FTIR spectra of the undamaged and X-ray-damaged PFSA. X-ray doses even as low as 5 MGy (area A) make detectable changes in the chemistry of the material, particularly when visualized with differential approaches. The infrared spectrum of PFSA and its assignment has been presented previously.[51,52] The FTIR spectrum of undamaged, partially hydrated PFSA (Figure 5a) contains two strong C−F stretches (1220, 1150 cm^{-1}) and three additional peaks at 982, 969, and 1058 cm^{-1}, which are attributed to a sulfonate stretch and two ether stretches corresponding to the terminal and linker side-chain ethers. Which of these peaks is assigned to the ethers and which to sulfonate remains controversial due to the potential presence of mechanically coupled vibrations and complex phase separation of the side chains. However, all features can be functionally understood as belonging to either the C−F backbone (1220 and 1150 cm^{-1}) or side-chain moieties (982, 969, and 1058 cm^{-1}). A higher-magnification view of the side-chain-related peaks is shown in Figure 5d. The limited signal quality when measuring small differences in ultrathin samples at high magnification makes the overlapping 969 and 982 cm^{-1} bands difficult to distinguish. These have been treated together as a single feature.

Vibrational spectroscopy reveals the bonding of the parent material and the radiation-damaged material that remains. To more sensitively examine the changes due to irradiation, differential absorbance spectra were examined and are plotted in Figure 5b.

$$\Delta Abs = \log(I_{damaged}/I_{undamaged})$$

where $I_{damaged}$ and $I_{undamaged}$ are the observed intensity of irradiated and reference PFSA, respectively. In these differential spectra, upward-going peaks indicate damage of the structural motif responsible for the vibrational transition. Negative-going peaks indicate that the radiation damage has created reaction products giving rise to new spectral features. A broad, negative-going peak centered at 1680 cm^{-1} is detected for all X-ray-damaged areas (inverted and magnified in Figure 5c), which is assigned to C=O and C=C bond stretches, in accordance with the NEXAFS images and previous work.[18] Supporting Figure S-9 presents histograms of the intensities of the integrated signals for the C−F, C−O-close, C−O-far, and C=O for the undamaged, and A, B, and C damaged regions, respectively.

FTIR spectroscopy indicates that the intensities of signals related to all of the bonds initially present in the PFSA (C−F, C−C, and side-chain-related oxygen bonds) are reduced by X-ray damage, and appear as positive-going peaks in the differential absorbance spectra, even for areas A and B given nominal doses of only 5 and 6 MGy. These bonds are broken, or, if still present, are in a changed molecular environment that has significantly changed the vibrational frequency. Loss of the broad signal between 1250 and 1350 cm^{-1}, which is attributed to C−C bonds or sulfonate dimers, was observed at all three doses. However, because of strong overlap, it was treated together with the more intense C−F stretch region.[53]

The NEXAFS and FTIR spectral information both show that PFSA exposed to X-rays contains new bonds (C=C and C=O) but the additional signal is much smaller than the lost signal, consistent with net fluorine atom loss. A major advantage of FTIR spectroscopy is its sensitivity to the ether and sulfonate vibrational modes, which have reduced intensity, clearly indicating significant damage to the side-chain moieties of PFSA. These changes are not very visible in the O 1s NEXAFS images (Figure 4c) in part due to the small amount of oxygen and thus low signal, and in part due to interference from oxygenated contaminants.[29]

3.4. Quantitative Evaluation of Changes Caused by X-ray Damage.

The results of quantitation of the spectral changes to STXM and FTIR are presented in Figures 6 and 7. The elemental changes determined by STXM (Figure 6a) are summarized in Table 2. There are negligible changes to the carbon content even for a nominal dose of 47 MGy. Although the oxygen decay does not seem significant as detected by STXM—11% elemental change for a nominal dose of 47 MGy—the rapid decay with increasing X-ray dose is much more visible for thicker samples (>150 nm).[20] Due to the limited OD and thus low sensitivity, as well as considerable evidence for oxygen-containing contaminants, the O 1s spectral change should be treated with caution. On the other hand, fluorine elemental loss is clearly detected even for low dose (regions A and B), where $10 \pm 3\%$ of the fluorine is lost, and $40 \pm 5\%$ of the fluorine is lost in region C.

The quantitation of the continuum signals at 320 and 710 eV follows similar trends to that observed in Figure 6a. Quantitative changes to the intensities of some specific NEXAFS transitions are presented in Table 3 and Figure 6b. Both the 292.4 and 690 eV peaks, related to the C−F bonds, decay approximately 10% for the low-dose regions (A, B) and almost 40% for region C.
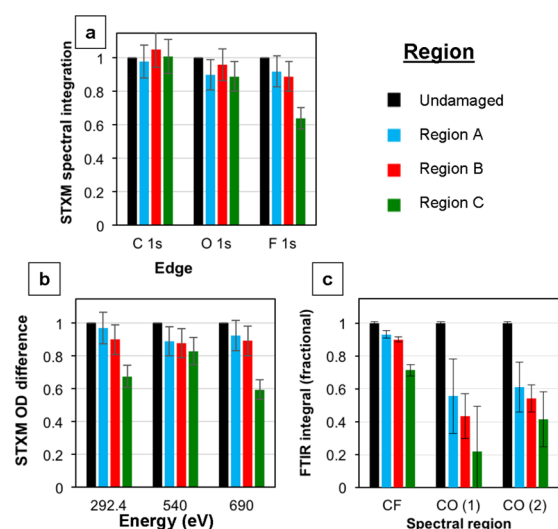
Figure 6. Quantitation of radiation-induced changes in the STXM and FTIR spectra associated with 320 eV X-ray damage with doses (from left to right) of the undamaged and damaged areas A, B, and C. (a) Elemental changes-integrated area of the background-subtracted C 1s, O 1s, and F 1s signals. (b) OD changes of peaks at 292.4 eV (C 1s → σ*$_{C-F}$), 540 eV (O 1s continuum), and 690 eV (F 1s → σ*$_{C-F}$), in each case after subtraction of preedge signal and normalization to the signal for undamaged PFSA. The error bars are the standard error. (c) Integrals of C−F, CO(1), and CO(2) peaks in the FTIR absorbance spectra. All data were normalized to the signal from the undamaged area so as to plot fractional differences.
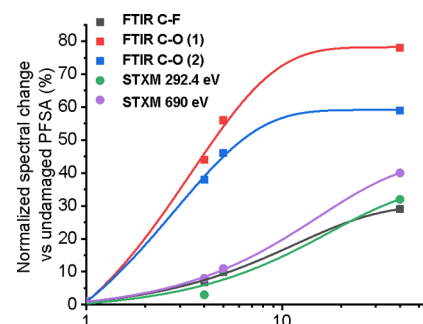
Figure 7. Comparison of the damage as a function of log(nominal dose), as measured by C 1s and F 1s NEXAFS images, and FTIR peak integral fractional changes. The solid lines are guides to the eye only.

Table 3. FTIR Integrals of Each Band, Normalized to the Intensity of Undamaged PFSA

area	% difference to undamaged area		
	C-F	C-O - 1	C-O - 2
A	6.8 (2.4)	44 (23)	38 (15)
B	9.9 (1.5)	56 (14)	46 (8)
C	29 (3.4)	78 (27)	59 (17)

For FTIR, each peak was numerically integrated, using an extrapolated baseline as discussed in Supporting Section SI-3. The integral of each band was compared to that for adjacent, undosed regions on the same sample to determine the percentage of X-ray-induced damage for each dose. The results are shown in Figure 6c. The C−F regions are much more accurately quantified because of their greater intensity. Consistent with the STXM results (Figure 6b and Tables 1−3), FTIR spectroscopy shows that approximately 10 and

35% of the C−F bonds are depleted with low (regions A and B)- and higher-dose (region C) X-ray exposures, respectively. It also shows that the ether depletion is quite severe even for low-dose STXM measurements (approximately 40% loss in the low-dose regions).

4. DISCUSSION

The dominant physical interaction of soft X-rays with matter is photoabsorption, which damages bonds both directly, when the inner shell excited or ionized state has a dissociative potential curve, and indirectly, through the inelastic scattering of secondary electrons (Auger, photoelectron, and cascade electrons).[54] In PFSA, the deposited energy triggers many outcomes, including bond breakage, bond formation, rearrangements, and mass loss.

We have shown with FTIR, AFM, and NEXAFS analyses that X-ray damage in PFSA leads to: (i) extensive fluorine mass loss, (ii) extensive damage to the organization of the C−F bonds, (iii) severe damage to the side chains, and iv) crosslinking, with formation of C=C and C=O bonds. In addition, there is evidence for ablation and redeposition of ablated material, although the results are somewhat ambiguous on this point. In polytetrafluoroethylene (PTFE, Teflon), the C−F bonds are broken by ionizing radiation, which produces a highly reactive fluorine radical that attacks the C−C bonds, producing C=C bonds.[55] It is likely that a similar process happens in the main chain of PFSA, which is essentially PTFE. However, the rate, as expressed by a first-order rate constant, is about 10 times faster in PFSA than in PTFE.[29]

It should be noted that the commercial PFSA used in this study is considered "chemically stabilized". This term usually implies that the polymer chain ends of the PFSA are terminated with CF_3 groups instead of COOH groups.[56] This modification enhances the chemical stability of the polymer versus radical attack. It also modifies the oxygen content, and presumably the initial presence of any C=O features in the FTIR spectra from chain ends. However, given the presence of the 289 eV peak in the C 1s spectrum, previously interpreted as corresponding to the transitions of C 1s → π^*_{COOH} of the COOX terminal groups,[49] it is likely that this PFSA sample is not completely free of these functionalities.

The changes in local viscoelasticity detected by AFM phase contrast imaging of the redeposited debris could be explained by intra- or interchain cross-linking or by oxidation of the damaged and ejected PFSA.[16,57] Cross-linking is also consistent with the formation of the C=C bonds detected by NEXAFS (Figure 4a) and by FTIR (Figure 5). Previous studies have identified carboxylic acids and C=C double bonds as the products of thermal and electrochemical degradation of PFSA.[58] The poorly defined nature of the product distribution prevents precise FTIR spectral analysis. The 1360 cm^{-1} feature detected in radiation-damaged PFSA could correspond to new C−C features in PTFE-like domains clipped free of side chains. Chain scission from γ-irradiation in PTFE and PFSA increases polymer crystallinity, and PTFE single crystals are observed to form spontaneously inside PFSA electron microscopy samples.[9]

The peak profile of the asymmetric C−F stretch (Figure 5, 1210 cm^{-1}) is substantially altered after irradiation, and displays a more complex pattern reflecting multiple overlapping C−F and C−C vibrations. The changes in the C−F peak profiles and relative intensities in the differential

absorbance spectra as a function of dose indicate that radiation-damaged PFSA evolves in a nonstoichiometric manner, and that different C−F bonds have different sensitivities toward beam damage.

Previous studies have concluded that the ether moieties are the points in PFSA most susceptible to chemical attack by radicals[59] and X-rays.[17] At 5 MGy nominal dose, the change of the CO(1) bands (1058 and 982 cm^{-1}) was twice as large as that of the C−F bands (1154 and 1214 cm^{-1}) (Figure 6). Precise kinetic analysis is limited by the signal-to-noise ratio of the small intensity of the side-chain bands as well as sampling at only two doses. No attempt was made to compensate for any preferential orientation of polymer backbone or side chains.[60] Control experiments with polarized IR beams showed good agreement with the unpolarized spectra, and searches for X-ray dichroism also indicated that the samples are isotropic (data not shown). For these reasons, FTIR integrals should be treated as semiquantitative. Side chains in PFSA are critical in shaping the morphology responsible for the unique properties of these polymers. Their evident sensitivity to radiation as measured by FTIR spectroscopy, but insensitivity as measured by NEXAFS, demonstrates the importance of measuring beam damage using a variety of experimental techniques. Because C−O vibrations associated with the side chain are more X-ray-sensitive than C−F vibrations (see Figure 6), fuel cell catalyst layers using ionomer with lower equivalent weight (higher side-chain content) are likely to exhibit enhanced damage kinetics with STXM imaging. It is anticipated that advanced PFSA ionomers[2] using "short side chains"[61] and ether-free side-chain linkages may show different behavior under STXM or TEM imaging.

STXM analysis shows a 30−40% reduction in the amount of elemental F and the intensity of the F 1s → σ^*(C−F) peak at 690 eV (Figures 6 and 7). In DuPont 521 with EW of 1100, there are ~40 fluorine atoms per sulfonic group, and 10 of those fluorine atoms belong to the part of the side chain between the ether closest to the backbone and the terminal sulfonic group. Assuming that preferential radiation damage to the side chain results in complete loss of these fluorine side-chain atoms, a large portion of the reduction in F signal observed at 40 MGy would be associated with side-chain loss, consistent with the FTIR results.

While not appropriate for direct structural determination, fluorescence imaging (Figure 1a) is useful as a nondamaging diagnostic technique. The catalytic decomposition of trace organic atmospheric species is apparently halted once side chains in the PFSA are destroyed by radiolysis. Of the analytical techniques in this study, fluorescence microscopy was the cheapest and fastest at imaging X-ray damage. However, it relies on the adventitious deposition of fluorescent contaminants, which is very likely lab-specific. Regions receiving only the dose from a large-area, defocused STXM stack appear bleached, as do the regions purposefully exposed to X-rays. Common techniques such as XPS, X-ray diffraction, or small-angle scattering often do not allow for a simple and precise measurement of beam position and spot size. UV-excited fluorescence imaging is a cheap and fast tool for mapping X-ray exposure, which will prove useful in checking for damage to ionomer by analytical methods using ionizing radiation.

The spectroscopy of X-ray-damaged PFSA suggests that the radiation-induced changes are similar to those caused by free radical degradation during fuel cell operation.[27] Electrochemi-

cally stressed membrane electrode assemblies (MEAs) studied by XPS showed fluorine depletion with increased graphitic carbon presence,[17] which is similar to our observations of X-ray-damaged PFSA using STXM and FTIR techniques. PFSA membranes chemically stressed under conditions which mimic fuel cell degradation exhibited side-chain disintegration, as studied with nuclear magnetic resonance spectroscopy.[62] To the extent that the damage phenomena involve similar radical chemistry, it might be possible to use radiation sensitivity to X-ray damage as a proxy for studying the durability of ionomer materials and their composites. While Fenton reagents have long been used for nonspecific radical attack,[57] STXM offers a more controlled exposure and built-in analytical capabilities. It is important that the dose is carefully monitored when studying aged or stress-tested fuel cell materials by STXM, to minimize the convolution of beam-induced damage with device-associated degradation.

Reasonable X-ray doses for these specimens depend on the specific application. As shown with AFM, FTIR, and NEXAFS analyses, high-quality (analytical) STXM measurements should strive to remain as low as possible so as to cause minimal physical and chemical damage to the fluorine content of PFSA materials. Preservation of the surface morphology, or delicate functionalities such as the side chains, requires even lower doses, probably below 1 MGy. We have recently claimed for electron beam studies that maximum dose should be <25 MGy for PFSA.[19] In this work, the higher sensitivity of FTIR and AFM suggests that radiation doses should be lower than 1 MGy for accurate quantitation studies, which truly do not damage the PFSA. Remaining below these limits requires special attention to microscope settings and efficient data collection strategies. These constraints severely restrict the analytical information that can be obtained from a given area with high spatial resolution. Fortunately, in STXM, the damage can be limited and the spatial resolution can be improved by recording images at only a few energies, which are chosen to optimize detection of specific components such as the PFSA ionomer in MEA electrodes.[7,8,21]

5. CONCLUSIONS

Soft X-ray damage to PFSA was characterized by NEXAFS, FTIR, fluorescence, and AFM analyses. PFSA materials are very sensitive to X-ray exposure and result in changes to their chemistry and physical morphology even at low nominal dose (5−6 MGy). We have shown that AFM is useful to visualize changes to the PFSA morphology and surface texture. NEXAFS and FTIR spectra capture an average perspective over a relatively larger sample volume. The fluorine mass loss detected by NEXAFS results in a thickness decay, as shown with AFM. Fluorescence microscopy was a facile technique for detecting irradiated areas, but could not discriminate dose or provide mechanistic insights. AFM was extremely effective in detecting the damage through topographic changes and visualizing ad-particles. Damage was observed for all bonds in PFSA visible with FTIR spectroscopy, consistent with NEXAFS, even at low imparted doses.

Quantitative analysis of the FTIR spectra revealed that side-chain moieties are more readily damaged than the polymer backbone, consistent with a mechanism involving radical scission. More work is required to understand the effects of radiation on the chemistry and morphology of polyelectrolytes. Developing efficient data collection strategies that minimize or even account for radiation damage is critical toward characterizing delicate samples at higher resolution and in 3D.

AUTHOR INFORMATION

Corresponding Author
*E-mail: aph@mcmaster.ca.

ORCID
Isaac Martens: 0000-0001-8342-6629
Lis G. A. Melo: 0000-0001-5427-1867
Dan Bizzotto: 0000-0002-2176-6799
Adam P. Hitchcock: 0000-0002-1598-7886

Present Address
[⊥]4D Labs, SFU, Burnaby, V5A 1S6 BC, Canada (L.G.A.M.).

Author Contributions
[∥]I.M. and L.G.A.M. contributed equally to this work.

Notes
The authors declare no competing financial interest.

REFERENCES

(1) Mauritz, K. A.; Moore, R. B. State of Understanding of Nafion. *Chem. Rev.* **2004**, *104*, 4535−4585.

(2) Kusoglu, A.; Weber, A. Z. New Insights into Perfluorinated Sulfonic-Acid Ionomers. *Chem. Rev.* **2017**, *117*, 987−1104.

(3) Schmidt-Rohr, K.; Chen, Q. Parallel Cylindrical Water Nanochannels in Nafion Fuel-Cell Membranes. *Nat. Mater.* **2008**, *7*, 75−83.

(4) Liu, J.; Suraweera, N.; Keffer, D. J.; Cui, S.; Paddison, S. J. On the Relationship between Polymer Electrolyte Structure and Hydrated Morphology of Perfluorosulfonic Acid Membranes. *J. Phys. Chem. C* **2010**, *114*, 11279−11292.

(5) Allen, F. I.; Comolli, L. R.; Kusoglu, A.; Modestino, M. A.; Minor, A. M.; Weber, A. Z. Morphology of Hydrated As-Cast Nafion Revealed through Cryo Electron Tomography. *ACS Macro Lett.* **2015**, *4*, 1−5.

(6) Susac, D.; Berejnov, V.; Hitchcock, A. P.; Stumper, J. STXM Study of the Ionomer Distribution in the PEM Fuel Cell Catalyst Layers. *ECS Trans.* **2011**, *41*, 629−635.

(7) Susac, D.; Berejnov, V.; Stumper, J.; Hitchcock, A. P. STXM Characterization of PEM Fuel Cell Catalyst Layers. *ECS Trans* 2013, *50*, 405−413.

(8) Melo, L. G. A.; Hitchcock, A. P.; Jankovic, J.; Stumper, J.; Susac, D.; Berejnov, V. Quantitative Mapping of Ionomer in Catalyst Layers by Electron and X-Ray Spectromicroscopy. *ECS Trans.* 2017, *80*, 275−282.

(9) Yakovlev, S.; Balsara, N. P.; Downing, K. H. Insights on the Study of Nafion Nanoscale Morphology by Transmission Electron Microscopy. *Membranes* 2013, *3*, 424−439.

(10) Cullen, D. A.; Koestner, R.; Kukreja, R. S.; Liu, Z. Y.; Minko, S.; Trotsenko, O.; Tokarev, A.; Guetaz, L.; Meyer, H. M.; Parish, C. M.; et al. Imaging and Microanalysis of Thin Ionomer Layers by Scanning Transmission Electron Microscopy. *J. Electrochem. Soc.* 2014, *161*, F1111−F1117.

(11) Ade, H.; Smith, A. P.; Cameron, S.; Cieslinski, R.; Mitchell, G.; Hsiao, B.; Rightor, E. X-Ray Microscopy in Polymer Science: Prospects of a 'New' Imaging Technique. *Polymer* 1995, *36*, 1843−1848.

(12) Ade, H.; Urquhart, S. NEXAFS Spectroscopy and Microscopy of Natural and Synthetic Polymers. *Adv. Ser. Phys. Chem.* 2002, *12*, 285−355.

(13) Ade, H.; Hitchcock, A. P. NEXAFS microscopy and resonant scattering: Composition and orientation probed in real and reciprocal space. *Polymer* 2008, *49*, 643−675.

(14) Hitchcock, A. P. Soft X-Ray Imaging and Spectromicroscopy. *Handbook on Nanoscopy*; Tendeloo, G. Van; Dyck, V. D.; Pennycook, S. J., Eds.; Wiley-VCH Verlag GmbH & Co. KGaA, 2012; Vol. *II*, pp 745−791.

(15) Wang, J.; Botton, G.; West, M.; Hitchcock, A. P. Quantitative Evaluation of Radiation Damage to Polyethylene Terephthalate by Soft X-Rays and High-Energy Electrons. *J. Phys. Chem. B* 2009, *113*, 1869−1876.

(16) Rightor, E. G.; Hitchcock, A. P.; Ade, H.; Leapman, R. D.; Urquhart, S. G.; Smith, A. P.; Mitchell, G.; Fischer, D.; Shin, H. J.; Warwick, T. Spectromicroscopy of Poly(Ethylene Terephthalate): Comparison of Spectra and Radiation Damage Rates in X-Ray Absorption and Electron Energy Loss. *J. Phys. Chem. B* 1997, *101*, 1950−1960.

(17) Schulze, M.; Lorenz, M.; Wagner, N.; Guelzow, E. XPS Analysis of the Degradation of Nafion. *Fresenius' J. Anal. Chem.* 1999, *365*, 106−113.

(18) Almeida, S. H.; Kawano, Y. Effects of X-Ray Radiation on Nafion Membrane. *Polym. Degrad. Stab.* 1998, *62*, 291−297.

(19) Melo, L. G. A.; Hitchcook, A. P. Electron Beam Damage of Perfluorosulfonic Acid Studied by Soft X-Ray Spectromicroscopy. *Micron* 2019, *121*, 8−20.

(20) Melo, L. G. A.; Hitchcook, A. P. Optimizing Soft X-Ray Spectromicroscopy for Fuel Cell Studies: X-Ray Damage of Ionomer. *Microsc. Microanal.* 2018, *24*, 460−461.

(21) Wu, J.; Melo, L. G. A.; Zhu, X.; West, M. M.; Berejnov, V.; Susac, D.; Stumper, J.; Hitchcock, A. P. 4D Imaging of Polymer Electrolyte Membrane Fuel Cell Catalyst Layers by Soft X-Ray Spectro-Tomography. *J. Power Sources* 2018, *381*, 72−83.

(22) Lee, V.; Susac, D.; Kundu, S.; Berejnov, V.; Atanasoski, R. T.; Hitchcock, A. P.; Stumper, J. STXM Characterization of Nano-structured Thin Film Anode Before and After Start-Up Shutdown and Reversal Tests. *ECS Trans.* 2013, *58*, 473−479.

(23) Lis, G. D. A.; Botton, G. A.; Hitchcock, A. P. Quantification of the Critical Dose for Radiation Damage to Perfluorosulfonic Acid Membranes Using Soft X-Ray Microscopy. *Microsc. Microanal.* 2015, *21*, 2443−2444.

(24) Wu, J.; Yuan, X. Z.; Martin, J. J.; Wang, H.; Zhang, J.; Shen, J.; Wu, S.; Merida, W. A Review of PEM Fuel Cell Durability: Degradation Mechanisms and Mitigation Strategies. *J. Power Sources* 2008, *184*, 104−119.

(25) Ramaswamy, N.; Hakim, N.; Mukerjee, S. Degradation Mechanism Study of Perfluorinated Proton Exchange Membrane

under Fuel Cell Operating Conditions. *Electrochim. Acta* 2008, *53*, 3279−3295.

(26) Xie, J.; Wood, D. L.; More, K. L.; Atanassov, P.; Borup, R. L. Microstructural Changes of Membrane Electrode Assemblies during PEFC Durability Testing at High Humidity Conditions. *J. Electrochem. Soc.* 2005, *152*, A1011.

(27) Hitchcock, A. P.; Berejnov, V.; Lee, V.; West, M.; Colbow, V.; Dutta, M.; Wessel, S. Carbon Corrosion of Proton Exchange Membrane Fuel Cell Catalyst Layers Studied by Scanning Transmission X-Ray Microscopy. *J. Power Sources* 2014, *266*, 66−78.

(28) Venkatesan, S. V.; Lim, C.; Holdcroft, S.; Kjeang, E. Progression in the Morphology of Fuel Cell Membranes upon Conjoint Chemical and Mechanical Degradation. *J. Electrochem. Soc.* 2016, *163*, F637−F643.

(29) Melo, L. G. A. Soft X-Ray Spectromicroscopy of Radiation Damaged Perfluorosulfonic Acid, Ph.D. Thesis, McMaster University, 2018.

(30) Paul, D. K.; Giorgi, J. B.; Karan, K. Chemical and Ionic Conductivity Degradation of Ultra-Thin Ionomer Film by X-Ray Beam Exposure. *J. Electrochem. Soc.* 2013, *160*, F464−F469.

(31) Berejnov, V.; Rubinstein, B.; Melo, L. G. A.; Hitchcock, A. P. First-Principles X-Ray Absorption Dose Calculation for Time-Dependent Mass and Optical Density. *J. Synchrotron Radiat.* 2018, *25*, 833−847.

(32) Zhang, X.; Jacobsen, C.; Lindaas, S.; Williams, S. Exposure Strategies for Polymethyl Methacrylate from in Situ X-Ray Absorption near Edge Structure Spectroscopy. *J. Vac. Sci. Technol., B: Microelectron. Nanometer Struct.–Process., Meas., Phenom.* 1995, *13*, 1477.

(33) Wang, J.; Morin, C.; Li, L.; Hitchcock, A. P.; Scholl, A.; Doran, A. Radiation Damage in Soft X-Ray Microscopy. *J. Electron Spectrosc. Relat. Phenom.* 2009, *170*, 25−36.

(34) Leontowich, A. F. G.; Hitchcock, A. P.; Tyliszczak, T.; Weigand, M.; Wang, J.; Karunakaran, C. Accurate Dosimetry in Scanning Transmission X-Ray Microscopes via the Cross-Linking Threshold Dose of Poly(Methyl Methacrylate). *J. Synchrotron Radiat.* 2012, *19*, 976−987.

(35) Coffey, T.; Urquhart, S. G.; Ade, H. Characterization of the Effects of Soft X-Ray Irradiation on Polymers. *J. Electron Spectrosc. Relat. Phenom.* 2002, *122*, 65−78.

(36) Leontowich, A. F. G. Utility of the G Value and the Critical Dose to Soft X-Ray Radiation Damage of Polyacrylonitrile. *Radiat. Phys. Chem.* 2013, *90*, 87−91.

(37) Wang, J. Radiation Chemistry by Soft X-Ray Spectromicroscopy, Ph.D. Thesis, McMaster University, 2008.

(38) Kilcoyne, A. L. D.; Tyliszczak, T.; Steele, W. F.; Fakra, S.; Hitchcock, P.; Franck, K.; Anderson, E.; Harteneck, B.; Rightor, E. G.; Mitchell, G. E.; et al. Interferometer-Controlled Scanning Transmission X-Ray Microscopes at the Advanced Light Source. *J. Synchrotron Radiat.* 2003, *10*, 125−136.

(39) Warwick, T.; Ade, H.; Kilcoyne, D.; Kritscher, M.; Tyliszczak, T.; Fakra, S.; Hitchcock, A.; Hitchcock, P.; Padmore, H. A New Bend-Magnet Beamline for Scanning Transmission X-Ray Microscopy at the Advanced Light Source. *J. Synchrotron Radiat.* 2002, *9*, 254−257.

(40) Kaznatcheev, K. V.; Karunakaran, C.; Lanke, U. D.; Urquhart, S. G.; Obst, M.; Hitchcock, A. P. Soft X-Ray Spectromicroscopy Beamline at the CLS: Commissioning Results. *Nucl. Instrum. Methods Phys. Res., Sect. A* 2007, *582*, 96−99.

(41) Melo, L. G. A.; Hitchcock, A. P.; Susac, D.; Stumper, J.; Berejnov, V. Effect of UV Radiation Damage in Air on Polymer Film Thickness, Studied by Soft X-Ray Spectromicroscopy. *Phys. Chem. Chem. Phys.* 2018, *20*, 16625−16640.

(42) Jacobsen, C.; Wirick, S.; Flynn, G.; Zimba, C. Soft X-Ray Spectroscopy from Image Sequences with Sub-100 Nm Spatial Resolution. *J. Microsc.* 2000, *197*, 173−184.

(43) Hitchcock, A. AXis 2000 Is Written in Interactive Data Language (IDL). It Is available free for non-commercial use from http://unicorn.mcmaster.ca/aXis2000.html (accessed April 19, 2019).

(44) Nečas, D.; Klapetek, P. Gwyddion: An Open-Source Software for SPM Data Analysis. *Cent. Eur. J. Phys.* **2012**, *10*, 181−188.

(45) Schindelin, J.; Arganda-Carreras, I.; Frise, E.; Kaynig, V.; Longair, M.; Pietzsch, T.; Preibisch, S.; Rueden, C.; Saalfeld, S.; Schmid, B.; et al. Fiji: an open-source platform for biological-image analysis. *Nat. Methods* **2012**, *9*, 676−682.

(46) Collete, F. M.; Lorentz, C.; Gebel, G.; Thominetter, F. Hydrothermal Aging of Nafion (R). *J. Membr. Sci.* **2009**, *330*, 21−29.

(47) PermaPure. Nafion: Physical and Chemical Properties, https://www.permapure.com/products/nafion-tubing/nafion-physical-and-chemical-properties/ (accessed April 19, 2019).

(48) Wetteland, C. J.; Gosnell, G.; Hollander, M. G.; Tesmer, J. R.; Mooday, R.; Wang, Y. Q. Ion Beam Irradiation of Polytetrafluoro-ethylene-Loaded Polyetheretherketone. *Nucl. Instrum. Methods Phys. Res., Sect. B* **2006**, *250*, 396−401.

(49) Yan, Z. B.; Hayes, R.; Melo, L. G. A.; Goward, G. R.; Hitchcock, A. P. X-Ray Absorption and Solid-State NMR Spectros-copy of Fluorinated Proton Conducting Polymers. *J. Phys. Chem. C* **2018**, *122*, 3233−3244.

(50) Urquhart, S. G.; Smith, A. P.; Ade, H. W.; Hitchcock, A. P.; Rightor, E. G.; Lidy, W. Near-Edge X-Ray Absorption Fine Structure Spectroscopy of MDI and TDI Polyurethane Polymers. *J. Phys. Chem. B* **1999**, *103*, 4603−4610.

(51) Webber, M.; Dimakis, N.; Kumari, D.; Fuccillo, M.; Smotkin, E. S. Mechanically Coupled Internal Coordinates of Ionomer Vibrational Modes. *Macromolecules* **2010**, *43*, 5500−5502.

(52) Cable, K. M.; Mauritz, K. A.; Moore, R. B. Effects of Hydrophilic and Hydrophobic Counterions on the Coulombic Interactions in Perfluorosulfonate Ionomers. *J. Polym. Sci., Part B: Polym. Phys.* **1995**, *33*, 1065−1072.

(53) Nagao, Y. Highly Oriented Sulfonic Acid Groups in a Nafion Thin Film on Si Substrate. *J. Phys. Chem. C* **2013**, *117*, 3294−3297.

(54) Baruchel, J. *Neutron and Synchrotron Radiation for Condensed Matter Studies: Theory, Instruments and Methods*; Baruchel, J., Hodeau, J.-L., Lehmann, M., Regnard, J.-R., Schlenker, C., Eds.; Springer-Verlag, 1993.

(55) Forsythe, J. S.; Hill, D. J. T. Radiation Chemistry of Fluoropolymers. *Prog. Polym. Sci.* **2000**, *25*, 101−136.

(56) Escobedo, G.; Raiford, K.; Nagarajan, G. S.; Schwiebert, K. E. Strategies for Mitigation of PFSA Polymer Degradation in PEM Fuel Cells. *ECS Trans.* **2005**, *1*, 303−311.

(57) Pugmire, D. L.; Wetteland, C. J.; Duncan, W. S.; Lakis, R. E.; Schwartz, D. S. Cross-Linking of Polytetrafluoroethylene during Room-Temperature Irradiation. *Polym. Degrad. Stab.* **2009**, *94*, 1533−1541.

(58) Feng, M.; Qu, R.; Wei, Z.; Wang, L.; Sun, P.; Wang, Z. Characterization of the Thermolysis Products of Nafion Membrane: A Potential Source of Perfluorinated Compounds in the Environment. *Sci. Rep.* **2015**, *5*, No. 9859.

(59) Ishimoto, T.; Koyama, M. A Review of Molecular-Level Mechanism of Membrane Degradation in the Polymer Electrolyte Fuel Cell. *Membranes* **2012**, *2*, 395−414.

(60) Ono, Y.; Nagao, Y. Interfacial Structure and Proton Conductivity of Nafion at the Pt-Deposited Surface. *Langmuir* **2016**, *32*, 352−358.

(61) Tant, M. R.; Darst, K. P.; Lee, K. D.; Martin, C. W. Structure and Properties of Short-Side-Chain Perfluorosulfonate Ionomers. In *Multiphase Polymers: Blends and Ionomers*; Utracki, L. A.; Weiss, R. A., Eds.; 1989; pp 370−400.

(62) Ghassemzadeh, L.; Kreuer, K. D.; Maier, J.; Müller, K. Chemical Degradation of Nafion Membranes under Mimic Fuel Cell Conditions as Investigated by Solid-State NMR Spectroscopy. *J. Phys. Chem. C* **2010**, *114*, 14635−14645.